



Carbon sources and sinks from an Ensemble Kalman Filter ocean data assimilation

M. Gerber¹ and F. Joos^{1,2}

Received 27 March 2009; revised 22 January 2010; accepted 19 February 2010; published 16 July 2010.

[1] We quantify contemporary and preindustrial net air-sea CO₂ fluxes by an Ensemble Kalman Filter assimilation of interior ocean observations and compare results with published estimates in the light of sensitivity to model transport and input data reconstructions. Four different published reconstructions of anthropogenic carbon and the ΔC_{gasex} tracer are assimilated into different versions of the Bern3D ocean model. The two tracers represent the components of dissolved inorganic carbon due to the anthropogenic perturbation and the air-sea gas exchange of preindustrial CO₂. Contemporary air-sea fluxes for broad latitudinal bands are consistent with those from earlier ocean inversions and the observed air-sea CO₂ partial pressure differences. We infer modest meridional transport rates of up to 0.5 GtC yr⁻¹ for the preindustrial and the contemporary ocean and a small carbon transport across the equator. The anthropogenic perturbation offsets the preindustrial net sea-to-air flux yielding a weak contemporary carbon sink in the Southern Ocean (south of 44°S) of 0.15 ± 0.25 GtC yr⁻¹. Preindustrial Southern Ocean outgassing varies by almost a factor of 2 among the four ΔC_{gasex} reconstructions. Large differences in regional fluxes are found between an earlier ocean inversion using Green's function and this study for the same model and input data calculation. Systematic differences in assimilated and optimized ΔC_{gasex} fields are large in both inversions, and the contemporary, anthropogenic, and preindustrial air-sea CO₂ flux in the high-latitude and midlatitude Southern Hemisphere remains uncertain.

Citation: Gerber, M., and F. Joos (2010), Carbon sources and sinks from an Ensemble Kalman Filter ocean data assimilation, *Global Biogeochem. Cycles*, 24, GB3004, doi:10.1029/2009GB003531.

1. Introduction

[2] Human activities cause atmospheric carbon dioxide (CO₂) and its radiative forcing to rise at a speed that is unprecedented for at least the last 20,000 years and well above the natural range of at least the past 800,000 years [Lüthi *et al.*, 2008; Joos and Spahni, 2008]. A quantitative understanding of the marine sources and sinks of CO₂ is an important element for understanding the role of the carbon cycle and climate-carbon cycle interactions in global warming projections [Denman *et al.*, 2007].

[3] The aim of this study is to quantify preindustrial and contemporary air-sea and meridional ocean carbon fluxes on the regional scale and to explore their uncertainties. It has been shown that the results of atmospheric inversion studies depend sensitively on details of the applied method [Kaminski *et al.*, 2001]. Unfortunately, only a very limited

set of ocean inversion studies exists that use a Green's function approach and the same ocean input data to infer contemporary air-sea fluxes [Jacobson *et al.*, 2007; Gruber *et al.*, 2009]. These studies reveal a large mismatch between assimilated and optimized data pointing to sensitivity to model transport and/or to input data. Thus, it appears timely to the test the sensitivity of ocean inversion results to the applied method and to the input data. Here we apply for the first time an Ensemble Kalman Filter method (EnKF) [Evensen, 2003] to assimilate ocean tracer data in the Bern3D model [Müller *et al.*, 2006] to estimates preindustrial and contemporary carbon fluxes, thereby complementing our earlier ocean inversion for anthropogenic carbon fluxes [Gerber *et al.*, 2009]. We systematically explore the joint uncertainty stemming from uncertainties from ocean transport and from tracer input data by using four ocean transport fields and four different published ocean tracer data sets. We provide a discussion on the differences in assimilated and optimized tracer data and highlight potential problems. We suggest that uncertainties in inferred air-sea fluxes have been underestimated in earlier ocean inversions that did not explicitly account for sensitivities to input data.

[4] The contemporary air-sea fluxes of CO₂ are conceptually often separated into "natural" and "anthropogenic" components to discuss and quantify physical and biogeo-

¹Climate and Environmental Physics, Physics Institute, University of Bern, Bern, Switzerland.

²Oeschger Centre for Climate Change Research, University of Bern, Bern, Switzerland.

chemical mechanisms driving carbon sources and sink fluxes and changes in carbon inventories. The natural part represents the air-sea flux before the beginning of the industrialization (~1750 AD), when the carbon cycle was relatively close to equilibrium on decadal to centennial timescales. The anthropogenic component is the perturbation from the preindustrial state.

[5] It has remained challenging to accurately quantify carbon sources and sink fluxes and underlying mechanisms, in part because of the large spatiotemporal variability of CO₂ fluxes [e.g., Bakker *et al.*, 2001], in part because it is not possible to measure the natural and anthropogenic components of the CO₂ air-sea flux, and of the carbon fluxes and stocks within the ocean separately.

[6] Major scientific efforts have been dedicated to quantify preindustrial and anthropogenic and contemporary carbon fluxes and stocks using both data and models. A set of studies aims to separate the preindustrial and anthropogenic component of the inorganic carbon in the ocean from tracer data and to reconstruct the detailed spatial distribution of preindustrial and anthropogenic carbon in the ocean [e.g., Chen and Millero, 1979; Heimann and Maier-Reimer, 1996; Gruber *et al.*, 1996; Sabine *et al.*, 2004; Álvarez *et al.*, 2009; Vázquez Rodríguez *et al.*, 2009], however, considerable discrepancies in Southern Ocean inventories are found between different observation-based methods [Álvarez *et al.*, 2009; Vázquez Rodríguez *et al.*, 2009].

[7] Another string of work is directed to establish the spatiotemporal distribution of the air-sea difference in the partial pressure of CO₂ (pCO₂) to calculate, in combination with an air-sea transfer velocity [e.g., Wanninkhof, 1992; Müller *et al.*, 2008], carbon fluxes [Tans *et al.*, 1990; Takahashi *et al.*, 2009].

[8] Alternatively, inverse approaches are utilized to infer inter alia contemporary air-sea fluxes of carbon from atmospheric and oceanic data in combination with transport models [e.g., Enting and Mansbridge, 1989; Gloor *et al.*, 2003; Baker *et al.*, 2006; Jacobson *et al.*, 2007; Rödenbeck *et al.*, 2008]. Inversions of the observed atmospheric CO₂ gradient yield agreement in flux for large latitudinal bands [Denman *et al.*, 2007], but reveal a large sensitivity of inferred regional fluxes to model details and suffer from the sparse CO₂ sampling network with 60–120 stations [Kaminski *et al.*, 2001]. In contrast, the oceanic carbon distribution has been established by thousands of measurements [Key *et al.*, 2004].

[9] Recently, the preindustrial and anthropogenic air-sea fluxes of CO₂ have been quantified from data-based reconstructions of C_{anth} and the tracer ΔC_{gasex} [Gloor *et al.*, 2003; Mikaloff Fletcher *et al.*, 2006, 2007; Gerber *et al.*, 2009]. The ΔC_{gasex} tracer reflects the component of the total inorganic carbon which is due to the preindustrial air-sea exchange of CO₂ (see section 2.1). Gruber *et al.* [2009], summarizing results from Mikaloff Fletcher *et al.* [2006, 2007], found in general consistency between the contemporary air-sea fluxes from the ocean inversion and the fluxes derived from the surface ocean partial pressure field of CO₂ [Takahashi *et al.*, 2009] and atmospheric inversions [Baker *et al.*, 2006].

[10] Sensitivity to input data or to ocean transport have been quantified [Mikaloff Fletcher *et al.*, 2006, 2007; Gerber *et al.*, 2009].

[11] Mikaloff Fletcher *et al.* [2006, 2007] use the Green's function of ten different ocean model or model setups to quantify uncertainties related to ocean transport. An area of concern is that the assimilated input data are not directly observed, but computed from oceanic tracer distributions using constant stoichiometric ratios. Mikaloff Fletcher *et al.* [2007] found that depth-dependent ratios strongly affect air-sea fluxes in regions that ventilate the deep ocean, most notably the Southern Ocean.

[12] Gerber *et al.* [2009] assessed uncertainties from systematic biases in the reconstructions of anthropogenic carbon (C_{anth}) by assimilating four global and six Atlantic reconstructions in their Ensemble Kalman Filter approach. The results indicate that the uptake and partitioning of carbon fluxes in the Southern Ocean remain uncertain and the explicit consideration of uncertainties in the C_{anth} reconstructions yields larger error bars for the inferred fluxes than derived by Mikaloff Fletcher *et al.* [2006] and discussed by Gruber *et al.* [2009].

[13] A disturbing feature of the inversion for preindustrial air-sea fluxes is the presence of substantial residuals in the ΔC_{gasex} tracer [Mikaloff Fletcher *et al.*, 2007; Gruber *et al.*, 2009] pointing to unsolved problems and rising a number of questions. How robust are inverse estimates for the Southern Ocean region where large discrepancies in reconstructed anthropogenic carbon are found? How do uncertainties in published data-based estimates of C_{anth} impact on the reconstruction of ΔC_{gasex} and preindustrial carbon fluxes?

2. Method

2.1. Data

[14] We use a quasi-conservative tracer, ΔC_{gasex} [Gruber and Sarmiento, 2002] to infer preindustrial air-sea CO₂ fluxes. The underlying hypothesis is that gradients in ΔC_{gasex} are only driven by air-sea CO₂ fluxes and by physical (advection, convection, diffusion) transport within the ocean. ΔC_{gasex} is computed from measured total inorganic carbon (C_T) by removing the reconstructed anthropogenic component C_{anth} , and the estimated signals from the remineralization of organic material and calcium carbonate by assuming constant stoichiometric ratios between carbon and phosphate, $r_{C:P}$, and between phosphate (PO_4^{3-}) and nitrate, $r_{N:P}$ in the remineralization flux of organic matter and a ratio of 0.5 between carbon and alkalinity (Alk) in calcium carbonate:

$$\Delta C_{gasex} = \frac{S_0}{S} (C_T - r_{C:P} PO_4^{3-} - 0.5(Alk + r_{N:P} PO_4^{3-}) - C_{anth} - const.) \quad (1)$$

[15] ΔC_{gasex} is computed for all available section data points of the GLODAP database [Key *et al.*, 2004] (<http://cdiac.esd.ornl.gov/oceans/glodap/GlopDV.htm>) and the values assigned to the appropriate grid cell of the Bern3D model.

$r_{C:P}$ and $r_{N:P}$ are set to 117 and 16 [Anderson and Sarmiento, 1994]. The constant $const$ is chosen to yield a mean surface concentration, or alternatively global ocean inventory, of zero. ΔC_{gasex} is normalized to a reference salinity $S_0 = 35$ psu. The anthropogenic perturbation is removed using four observation-based reconstructions of C_{anth} . The C_{anth} estimates from the ΔC^* , TTD and CFC shortcut reconstructions are available from the GLODAP site. The TrOCA C_{anth} estimates are calculated following Touratier et al. [2007] from the GLODAP section data.

[16] A detailed comparison of different C_{anth} data can be found in the work of Vázquez Rodríguez et al. [2009], a short overview of the methods is presented by Gerber et al. [2009], and further details are available from the original publications [Gruber et al., 1996; Thomas and Ittekkot, 2001; Waugh et al., 2006; Touratier et al., 2007]. Three of the reconstruction methods (ΔC^* , TTD and CFC shortcut) have been investigated in the framework of an OGCM [Matsumoto and Gruber, 2005; Waugh et al., 2006; Matear et al., 2003]. The ΔC^* method shows a tendency toward overestimation of C_{anth} in young water masses, but underestimation in old water [Matsumoto and Gruber, 2005]. The TTD method tends to be biased high in the Southern Ocean due to the assumed temporally constant air-sea CO_2 disequilibrium [Waugh et al., 2006]. The CFC shortcut method is not very reliable for old water masses such as those in the deep ocean and those found in the Southern Ocean [Matear et al., 2003; Waugh et al., 2006]. Two recent studies comparing different C_{anth} reconstructions in the Atlantic and the Indian suggest that the ΔC^* method yields too low C_{anth} inventories in the Southern Ocean [Vázquez Rodríguez et al., 2009; Álvarez et al., 2009].

2.2. Model Setup

2.2.1. Optimization Scheme

[17] The approach of Gerber et al. [2009] is used with a few adaptation and a brief overview is given next. Further detail are found elsewhere [Gerber et al., 2009; Evensen, 2003, 2004]. The global ocean surface of the Bern3D model is divided into 17 regions (Figure S1).¹ Due to strong correlations between the inferred fluxes from the southern subpolar regions (Region nr. 8 and 15) and from the polar Southern Ocean region (Region nr. 9) (Figure S1), we have aggregated these regional fluxes to a single regional flux, which is labeled “Southern Ocean”. The air-sea flux of CO_2 for each model region F_l is described as the product of a spatiotemporal pattern, $P(i, j, t)$, and a scaling parameter, ψ :

$$F_l(i, j, t) = P(i, j, t)\psi(l) \quad (2)$$

[18] P is scaled to a unit flux (integrated over the region and year). ψ is the magnitude of the air-sea flux as optimized in the EnKF analysis scheme for each region l . The seasonal pattern $P(i, j, t)$ is based on the CO_2 air-sea flux climatology of Takahashi et al. [2002].

¹Auxiliary materials are available in the HTML. doi:10.1029/2009GB003531.

[19] The air-sea fluxes of carbon act as a source or sink of ΔC_{gasex} in the Bern3D model. ΔC_{gasex} is transported as a conservative tracer within the model ocean. After spin up of the circulation, the Bern3D is initialized with a ΔC_{gasex} concentration of zero and integrated over 3000 years.

[20] In the EnKF, an ensemble of 32 members is applied and each member is forced with a set of the 17 flux scaling parameters ψ_l . The ensemble members are optimized in a way that minimizes the deviation between data-based estimates and modeled distribution of the ΔC_{gasex} tracer. The optimization is repeated until convergence of the solution, typically reached after a few iteration steps. Convergence is defined as the rate change of the ensemble mean and ensemble standard deviation over the last three iteration steps. We applied a convergence criterion of 5%. The initial scaling parameters for any region are normally distributed around zero having a standard deviation of about 0.3 GtC yr^{-1} . We have not explicitly added a process noise. The ensemble size has been tested in a simulation, where we included 64 instead of 32 ensemble members. Deviations in the inferred air-sea fluxes are less than 0.05 GtC yr^{-1} , except for the Southern Ocean, where we find a deviation up to 0.08 GtC yr^{-1} . The root-mean-square error (RMSE) between optimized and observation-based ΔC_{gasex} remains the same.

2.2.2. Bern3D Model Configurations

[21] The Bern3D ocean model [Müller et al., 2006] is a cost efficient global circulation model with 36×36 (horizontal) \times 32 (vertical) boxes and is based on the ocean model of Edwards and Marsh [2005]. Model results are found to be in good agreement with observed distribution of different tracers [Müller et al., 2006, 2008; Parekh et al., 2008; Tschumi et al., 2008]. As in the work of Gerber et al. [2009], four different model setups with different circulation patterns or mixing are used to assess sensitivities associated to ocean transport. These have been built to investigate existing shortcomings in the circulation of the Bern3D model. Figure S2 shows the overturning and the different circulation setups are described in the caption. The Green’s function of the standard setup has been used earlier in the inversions of Mikaloff Fletcher et al. [2006, 2007]. The skill of the Bern3D model in representing the observation-based radiocarbon distribution compares with a score of 0.93 favorably to that of general circulation ocean models with a range of skill scores from 0.65 to 0.94 [Mikaloff Fletcher et al., 2007].

2.3. Calculation of Contemporary Air-Sea Fluxes and Best Estimates

[22] Contemporary air-sea fluxes for each region are calculated as the sum of the preindustrial fluxes inferred from the ΔC_{gasex} tracer, the anthropogenic air-sea fluxes of Gerber et al. [2009] for the nominal year 1995, and a river-derived outgassing taken from Jacobson et al. [2007] and as used by Gruber et al. [2009]. The input of organic and inorganic carbon by rivers causes an outgassing of CO_2 [Sarmiento and Sundquist, 1992] and causes a gradient in ΔC_{gasex} . The Ensemble Kalman Filter (EnKF) inversion interprets this gradient as an air-sea flux for which a correction is needed. We assume steady state condition for ocean circulation and biogeochemistry since the beginning

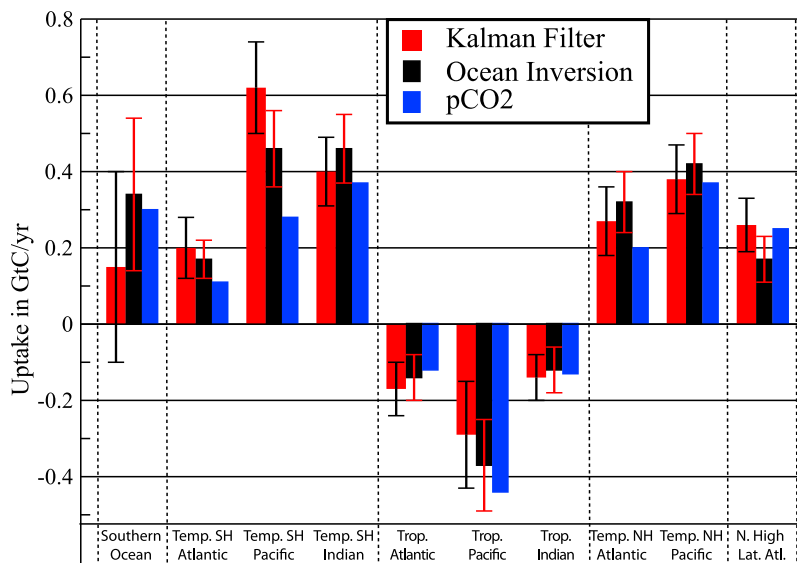


Figure 1. Contemporary net air-to-sea fluxes of CO_2 for aggregated regions as inferred by assimilating ocean tracer data into the Bern3D transport model (red). Error bars represent ± 1 standard deviation and include sensitivities to input data, ocean transport, and river-derived outgassing. Results obtained by the Green's function ocean inversion of Mikaloff Fletcher *et al.* [2006, 2007] (black) and from a climatology of the air-sea CO_2 partial pressure difference [Takahashi *et al.*, 2009] as published by Gruber *et al.* [2009] (blue) are shown for comparison.

of the industrialization and calculate the contemporary air-sea fluxes from the inferred preindustrial, anthropogenic, and riverine fluxes.

[23] Best estimates are calculated by averaging the results obtained for the four different ΔC_{gasex} fields. Individual estimates are weighted using the same skill score as Gerber *et al.* [2009] and derived from the assimilated and modeled C_{anth} fields. For ocean transport and river outgassing, we apply the same uncertainties as Gruber *et al.* [2009]. Overall uncertainties are estimated by adding uncertainties from the ΔC_{gasex} input data, ocean transport, and river-driven outgassing using Gaussian error propagation. All uncertainties provided represent ± 1 standard deviation.

3. Results

3.1. Large-Scale Carbon Sources and Sink Fluxes

[24] The results of the EnKF inversion are aggregated for each basin into broad latitudinal bands to ease comparison with other studies. The aggregated Bern3D-EnKF inversion yields the familiar pattern of outgassing of CO_2 in the tropics and ocean uptake in the temperate and high-latitude ocean (Figure 1). The contemporary (1995 AD) tropical source (19°S to 16°N) is estimated to be $0.60 \pm 0.16 \text{ GtC yr}^{-1}$. The contemporary high-latitude sinks are $0.15 \pm 0.25 \text{ GtC yr}^{-1}$ in the Southern Ocean and $0.25 \pm 0.07 \text{ GtC yr}^{-1}$ in the northern North Atlantic. The sink in the midlatitude ocean amounts to $1.20 \pm 0.16 \text{ GtC yr}^{-1}$ in Southern and to $0.64 \pm 0.13 \text{ GtC yr}^{-1}$ in the Northern Hemisphere.

[25] The attribution of the contemporary fluxes to a preindustrial flux (natural plus riverine outgassing), and to an anthropogenic perturbation reveals underlying oceanographic

mechanisms (Table 1 and Figure S3). The perturbation flux is into the ocean in all regions, with largest sink fluxes of C_{anth} into the Southern Ocean. At preindustrial time, the inferred tropical source is larger than today, whereas the temperate and northern high-latitude sink fluxes are considerably smaller than today. In the Southern Ocean, the preindustrial component corresponds to a source of $0.69 \pm 0.15 \text{ GtC yr}^{-1}$ that is more than offset by an uptake flux of $0.86 \pm 0.25 \text{ GtC yr}^{-1}$ of C_{anth} .

[26] The flux patterns are consistent with the generally accepted picture of ocean circulation and the observed surface temperature and nutrient distributions. The preindustrial pattern is the result of the interplay of the solubility pump and the biological pump [Maier-Reimer, 1993; Murnane *et al.*, 1999; Sarmiento *et al.*, 2000]. Warming causes the $p\text{CO}_2$ to rise favoring outgassing in the warm tropical region and uptake in the midlatitude and high-latitude ocean. Formation of organic material tends to lower $p\text{CO}_2$, whereas remineralization tends to enhance $p\text{CO}_2$. Consequently, we expect a tendency toward CO_2 outgassing in regions where nutrient and carbon rich water is brought to the surface and uptake from the atmosphere where organic matter is formed. Thus, the CO_2 outgassing in the tropics and in the Southern Ocean is explained by upwelling of nutrient rich waters, whereas the sink in midlatitude regions and in the high-latitude North Atlantic is consistent with the low nutrient concentrations and with cooling of poleward flowing waters.

[27] In the inversion, the preindustrial air-sea flux is a direct consequence of the gradients in ΔC_{gasex} and ocean model transport. For example, Circumpolar Deep Water (CPDW) with high ΔC_{gasex} concentrations is transported toward the surface, moving northward by the Ekman drift

Table 1. Regional Net Air-to-Sea Fluxes of CO₂ for the Anthropogenic Perturbation, the Preindustrial Time, and the Present^a

Region	C _{anth}	This Study		Mikaloff Fletcher et al. [2007]			Takahashi et al. [2008], Total
		Preindustrial	Total	C _{anth}	Preindustrial	Total	
Atlantic N. High Lat.	0.13 ± 0.06	0.16 ± 0.04	0.25 ± 0.07	0.09 ± 0.04	0.11 ± 0.02	0.17 ± 0.06	0.25
Atlantic N. Midlat.	0.10 ± 0.05	0.02 ± 0.05	0.11 ± 0.06	0.13 ± 0.04	0.12 ± 0.04	0.24 ± 0.06	0.15
Atlantic N. Low Lat.	0.04 ± 0.05	0.16 ± 0.04	0.16 ± 0.06	0.04 ± 0.04	0.08 ± 0.04	0.08 ± 0.06	0.05
Atlantic N. Tropics	0.03 ± 0.02	-0.11 ± 0.02	-0.17 ± 0.05	0.04 ± 0.02	-0.03 ± 0.01	-0.08 ± 0.05	-0.03
Atlantic S. Tropics	0.11 ± 0.03	-0.09 ± 0.02	0 ± 0.04	0.09 ± 0.02	-0.14 ± 0.02	-0.06 ± 0.03	-0.09
Atlantic S. Low Lat.	0 ± 0.01	0 ± 0.01	0 ± 0.01	0.02 ± 0.01	-0.02 ± 0.01	0.01 ± 0.01	-0.02
Atlantic S. Midlat.	0.05 ± 0.04	0.17 ± 0.08	0.19 ± 0.08	0.05 ± 0.02	0.11 ± 0.05	0.16 ± 0.05	0.13
Pacific N. High Lat.	0.05 ± 0.03	0 ± 0.04	0.02 ± 0.05	0.04 ± 0.01	-0.02 ± 0.04	0 ± 0.04	0.12
Pacific N. Midlat.	0.05 ± 0.06	0.25 ± 0.06	0.35 ± 0.08	0.15 ± 0.04	0.31 ± 0.05	0.42 ± 0.07	0.37
Pacific N. Tropics	0.18 ± 0.05	-0.30 ± 0.06	-0.15 ± 0.08	0.18 ± 0.04	-0.22 ± 0.06	-0.06 ± 0.07	-0.12
Pacific S. Tropics	0.12 ± 0.05	-0.25 ± 0.08	-0.14 ± 0.10	0.11 ± 0.02	-0.41 ± 0.08	-0.31 ± 0.09	-0.32
Pacific S. Midlat.	0.09 ± 0.06	0.52 ± 0.10	0.61 ± 0.11	0.11 ± 0.04	0.36 ± 0.09	0.46 ± 0.10	0.28
Indian Tropics	0.07 ± 0.04	-0.12 ± 0.03	-0.14 ± 0.06	0.11 ± 0.03	-0.14 ± 0.02	-0.12 ± 0.06	-0.13
Indian S. Midlat.	0.12 ± 0.12	0.29 ± 0.12	0.40 ± 0.09	0.25 ± 0.08	0.22 ± 0.06	0.46 ± 0.09	0.37
Southern Ocean	0.86 ± 0.25	-0.69 ± 0.15	0.15 ± 0.25	0.74 ± 0.17	-0.40 ± 0.11	0.34 ± 0.20	0.30
Global	2.10 ± 0.30	-0.01 ± 0.09	1.67 ± 0.38	2.18 ± 0.25	-0.05 ± 0.08	1.70 ± 0.35	1.31

^aUnits are GtC yr⁻¹. Fluxes of this study are compared to those from the ocean inversion of Mikaloff Fletcher et al. [2006, 2007] and those derived from a climatology of the air-sea CO₂ partial pressure difference [Takahashi et al., 2009] as published by Gruber et al. [2009]. Fluxes of this study represent weighted averages of the fluxes shown in Table 3 for four different reconstructions of C_{ant} and ΔC_{gasex}. Uncertainties represent ±1 standard deviation. Uncertainties in this study include those from sensitivities to input data, ocean transport, and river-driven outgassing which are added according Gaussian error propagation, whereas uncertainties from Mikaloff Fletcher et al. [2006, 2007] do not include uncertainties from different input data.

and subsequently transformed into Antarctic Intermediate Water (AAIW). Thus, the decrease in ΔC_{gasex} concentration of order 50 μmol between CPDW to AAIW is due to the strong CO₂ outgassing in the Southern Ocean and partly due to mixing with other water masses.

[28] Turning to the anthropogenic perturbation, the accelerating atmospheric CO₂ growth causes a positive perturbation in the surface atmosphere-ocean partial pressure difference relative to the natural, preindustrial situation and uptake of C_{anth} in all regions. The uptake of C_{anth} is expected to be particularly large in regions were “old” water, that has a low concentration of C_{anth} and a large potential for C_{anth} uptake, is upwelled or mixed by convection into the surface. A confounding factor is warming and cooling. Warming has the tendency to enhance C_{anth} uptake as the Revelle factor is lower and thus the uptake capacity for C_{anth} is higher for warm than for cold water. The strong anthropogenic uptake flux in the Southern Ocean appears to be driven by upwelling of Circumpolar Deep Water and subsequent warming as the water is moved northward by the Ekman drift before being subducted as AAIW and Subantarctic Mode Water (SAMW). Uptake fluxes per unit area are also relatively high in the upwelling regions of the tropics and in the Nordic Seas where convection and North Atlantic Deep Water formation carry C_{anth} efficiently to the abyss. (Figure S2).

[29] The reconstructed contemporary fluxes for broad latitudinal bands of individual ocean basins are broadly consistent with the results of the Green’s function ocean inversion (GFOI) [Gruber et al., 2009], the fluxes from the pCO₂ climatology [Takahashi et al., 2009], and the atmospheric inversion of Baker et al. [2006]. The EnKF results agree with the results from the GFOI for each aggregated region within their uncertainties. Differences between the two studies are large for the Southern Ocean and the Pacific midlatitude region.

[30] The EnKF inversion, as well as the GFOI, yield higher contemporary uptake fluxes in the southern midlatitudes than the pCO₂ climatology. The disagreement is particularly striking for the temperate Pacific region, a region where sampling density for the pCO₂ climatology is low [Takahashi et al., 2009].

[31] Interestingly, the atmospheric inversion of Baker et al. [2006] suggests a small net sea-to-air flux in the mid-latitude Southern Pacific, a finding that is in strong contrast to the uptake flux inferred by all oceanographic methods.

3.2. Uncertainties in Inferred Preindustrial Air-Sea CO₂ Fluxes

3.2.1. Sensitivity of Preindustrial Air-Sea Fluxes to Ocean Transport and Prescribed Seasonal Flux Pattern

[32] Four different circulation setups of the Bern3D ocean model are applied each with two different ΔC_{gasex} data. These are computed by removing the anthropogenic signal reconstructed with the ΔC* and the TTD method [Gruber et al., 1996; Waugh et al., 2006] and by normalizing the ΔC_{gasex} field to have zero average surface concentration. A few regions are particularly sensitive to changes in circulation: the Southern Ocean, the high-latitude North Atlantic, and the southern midlatitude regions (Table 2).

[33] Air-sea fluxes from both reconstruction methods, i.e., ΔC* and TTD, show a similar sensitivity to altered circulation fields. The more vigorous Atlantic overturning and the deeper penetration of NADW in the “ACC” and “PSI × 3” setups leads to a higher uptake flux in the high-latitude and midlatitude North Atlantic. The inferred uptake flux north of 34°N in the Atlantic is more than twice as high for these two settings than for the standard setup. Consequently, the export of ΔC_{gasex} from the deep North Atlantic to the Southern Hemisphere is enhanced.

[34] The enhanced strength of the circumpolar currents causes a more vigorous exchange between the Southern

Table 2. Regional Net Air-to-Sea Fluxes of Natural CO₂ for Four Different Bern3D Transport Versions and Two Modified Setups With the Standard Bern3D Model^a

Region	Area in 10 ⁶ km ²	ΔC^* Reconstructions							TTD Reconstructions			
		Standard	ACC \times 3	PSI \times 3	High Diffusion	Seasonally Forced	Zero Inventory	Ocean Inversion	Standard	ACC \times 3	PSI \times 3	High Diffusion
Atlantic N. High Lat.	9.45	0.21	0.32	0.43	0.21	0.12	0.18	0.14	0.19	0.27	0.37	0.19
Atlantic N. Midlat.	11.81	-0.01	0.10	0.09	0.02	0.07	0	0.09	0.01	0.14	0.15	0.05
Atlantic N. Low Lat.	16.53	0.16	0.15	0.14	0.13	0.15	0.15	0.09	0.17	0.16	0.12	0.13
Atlantic N. Tropics	14.17	-0.10	-0.11	-0.11	-0.13	-0.09	-0.09	-0.03	-0.12	-0.13	-0.12	-0.15
Atlantic S. Tropics	10.23	-0.06	-0.09	-0.10	-0.06	-0.10	-0.09	-0.10	-0.09	-0.1	-0.12	-0.08
Atlantic S. Low Lat.	10.23	0	0	0	0	0	0	-0.01	0.01	0	0	0.01
Atlantic S. Midlat.	9.45	0.23	0.14	0.13	0.19	0.09	0.21	0.05	0.11	0.05	0.02	0.08
Pacific N. High Lat.	12.20	-0.02	-0.01	0.0	-0.004	-0.02	-0.01	0.01	-0.01	0.01	0.01	0.02
Pacific N. Midlat.	37.78	0.28	0.27	0.28	0.29	0.26	0.25	0.20	0.26	0.26	0.28	0.28
Pacific N. Tropics	38.96	-0.28	-0.30	-0.32	-0.35	-0.30	-0.29	-0.18	-0.29	-0.3	-0.33	-0.38
Pacific S. Tropics	28.33	-0.26	-0.26	-0.26	-0.20	-0.25	-0.24	-0.44	-0.29	-0.32	-0.3	-0.22
Pacific S. Midlat.	39.36	0.45	0.57	0.60	0.46	0.44	0.48	0.47	0.52	0.65	0.65	0.53
Indian Tropics	31.88	-0.10	-0.11	-0.12	-0.10	-0.10	-0.11	-0.11	-0.11	-0.11	-0.12	-0.10
Indian S. Midlat.	24.01	0.22	0.25	0.27	0.21	0.17	0.26	0.11	0.20	0.22	0.23	0.18
Southern Ocean	58.64	-0.53	-0.72	-0.83	-0.47	-0.46	-0.72	-0.32	-0.40	-0.58	-0.62	-0.36
Global		0.19	0.20	0.20	0.20	-0.02	-0.01	-0.03	0.16	0.21	0.21	0.19
RMSE ΔC_{gasex} ($\mu\text{mol } \Gamma^{-1}$)		17.82	15.29	14.15	16.94	17.27	16.86	18.70	17.31	14.86	14.60	16.53
Correlation		0.66	0.76	0.77	0.69	0.68	0.7	0.66	0.68	0.77	0.78	0.71

^aUnits are in GtC yr⁻¹. Natural CO₂ is preindustrial without river-derived. The root mean square error (RMSE) and correlation between optimized and data-based fields of ΔC_{gasex} are calculated using all data points assimilated to the optimization. The column “zero inventory” shows the air-sea fluxes inferred from reconstruction with an offset such that the total inventory of the ΔC_{gasex} is zero (see equation (1)). The “seasonally forced” column shows air-sea fluxes with a modified flux pattern in the northern high Atlantic and Southern Ocean to increase the uptake during the winter months. The “Ocean Inversion” column shows the results from the Bern3D model given by *Mikaloff Fletcher et al.* [2007] who used a slightly different grid than used in this study. (Deviations in area are up to 15%.)

Ocean and the midlatitude ocean, enhancing uptake in the midlatitude Pacific and midlatitude Indian regions and outgassing in the Southern Ocean.

[35] The increased uptake in the North Atlantic and the Pacific and Indian southern midlatitude regions is mostly balanced by enhanced outgassing in the Southern Ocean region by 0.19 and 0.30 GtC yr⁻¹ (ΔC^*), (0.18 and 0.22 GtC yr⁻¹ for the TTD), and a decrease in the aggregated net air-to-sea flux in the midlatitude and tropical Atlantic (46°S to 34°N) by 0.14 and 0.18 (ΔC^*), (0.1 and 0.1 GtC yr⁻¹ for the TTD) relative to the standard setup.

[36] Increasing vertical diffusivity for passive tracers by a factor of 4 has a small effect (<0.09 GtC yr⁻¹) on inferred sources and sinks (Table 2).

[37] Observation-based concentrations of ΔC_{gasex} are much higher than model results in the deep Pacific and Atlantic (Figure 2). We have modified the seasonal pattern for the northern high-latitude Atlantic and for the polar Southern Ocean toward larger uptake rates during the winter time and less uptake or even outgassing during summer time. Thereby, we tend to increase the ΔC_{gasex} concentrations in the surface during times of deep water formation in the Nordic Seas and the Southern Ocean and to reduce the data-model difference in the deep.

[38] Technically, the seasonal pattern of the two regions has been shifted by an offset of $0.95 \times \bar{p}_n$ where \bar{p}_n is the temporal and spatial average flux of each grid box:

$$\tilde{p}(i,j,t)_n = \frac{p(i,j,t)_n - 0.95\bar{p}}{\int_{i,j,t} (p(i,j,t) - 0.95\bar{p})} \quad (3)$$

We emphasize that there is no reason to modify the prescribed spatiotemporal pattern from the pCO₂ climatology in such a drastic way and that this modification represents an extreme case. The inferred uptake pattern in the North Atlantic is changing toward less uptake in the North Atlantic high-latitude region, entirely compensated by increased uptake in the northern midlatitude region. The Southern Ocean outgassing is reduced by 0.07 GtC yr⁻¹ relative to the standard and uptake in the Atlantic southern midlatitude region is reduced from 0.23 to 0.09 GtC yr⁻¹, whereas results are similar as in the standard setup for other regions.

[39] The modification in seasonal forcing did not improve the modeled distribution of ΔC_{gasex} and residuals in the deep Atlantic and deep Pacific are still high. Thus, a potential mismatch in the seasonality of the air-sea flux and ocean transport is not an explanation for the large residuals.

[40] An intriguing finding of this first set of sensitivity simulations is that the global average air-sea CO₂ flux does not vanish. The inversion yields a global uptake flux of 0.2 GtC yr⁻¹ (Table 2). This is inconsistent with the assumption of an ocean in steady state at preindustrial time. We attribute this to the choice of the normalization constant in the computation of ΔC_{gasex} . Following earlier work, the constant has been set to yield an average surface concentration of zero and a whole ocean inventory of the ΔC_{gasex} tracer of around 600 GtC. The implication is that a global uptake of 0.2 GtC yr⁻¹ is required in our 3000 year long simulations to match the global ΔC_{gasex} inventory.

[41] The ΔC_{gasex} field is renormalized to yield a zero ocean inventory to avoid the implicit requirement of a net

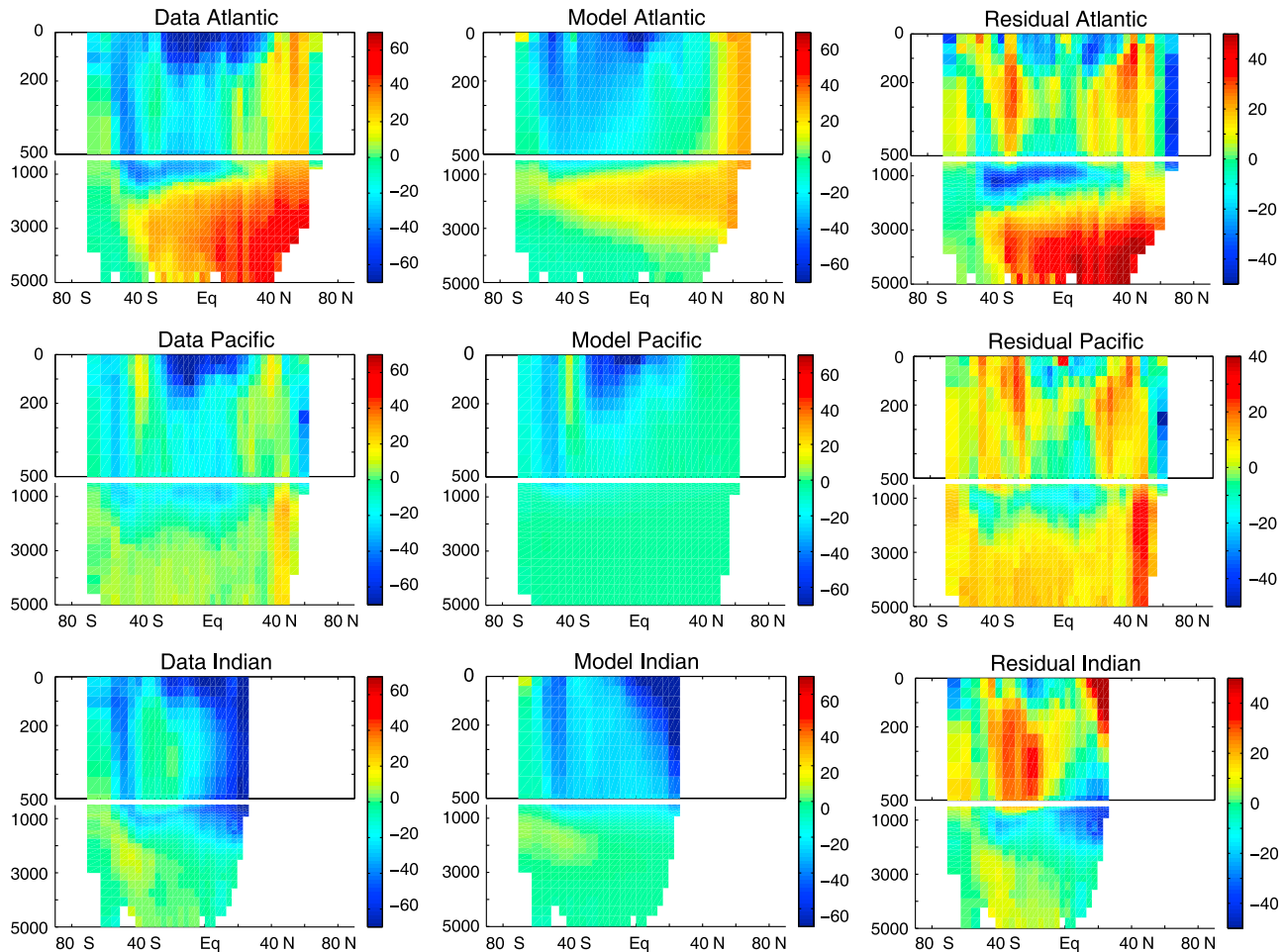


Figure 2. Zonal average of data-based and modeled distribution (standard setup) of ΔC_{gasex} (ΔC^* with zero inventory normalization) and of the corresponding residuals (data minus model) in $\mu\text{mol l}^{-1}$ for the Atlantic, Pacific, and Indian oceans.

ocean uptake. This is permissible as ocean tracer transport is described by a set of linear equations and the addition of a constant does not change tracer divergence. As expected, the global net air-sea flux is reduced close to zero in the EnKF (Table 2). Surprisingly, this reduction is almost entirely achieved by an increase in Southern Ocean outgassing by 0.19 GtC yr^{-1} . The GFOI approach does not show a similar strong sensitivity of the results to the normalization constant, the inclusion of the normalization constant in the set of optimized parameters revealed only a small sensitivity of the inferred air-sea fluxes (S. E. Mikaloff-Fletcher, personal communication).

[42] In summary, in the EnKF approach, the air-sea flux for the Southern Ocean region appears to be particularly sensitive for the details of the model setup and the ΔC_{gasex} field should preferentially be normalized to yield a zero global inventory. We note that the results presented in the figures and in Tables 1 and 3 and further discussed below have all been obtained by applying ΔC_{gasex} fields normalized to a zero inventory.

3.2.2. Sensitivity of Preindustrial Air-Sea Fluxes to Different Reconstructions of ΔC_{gasex}

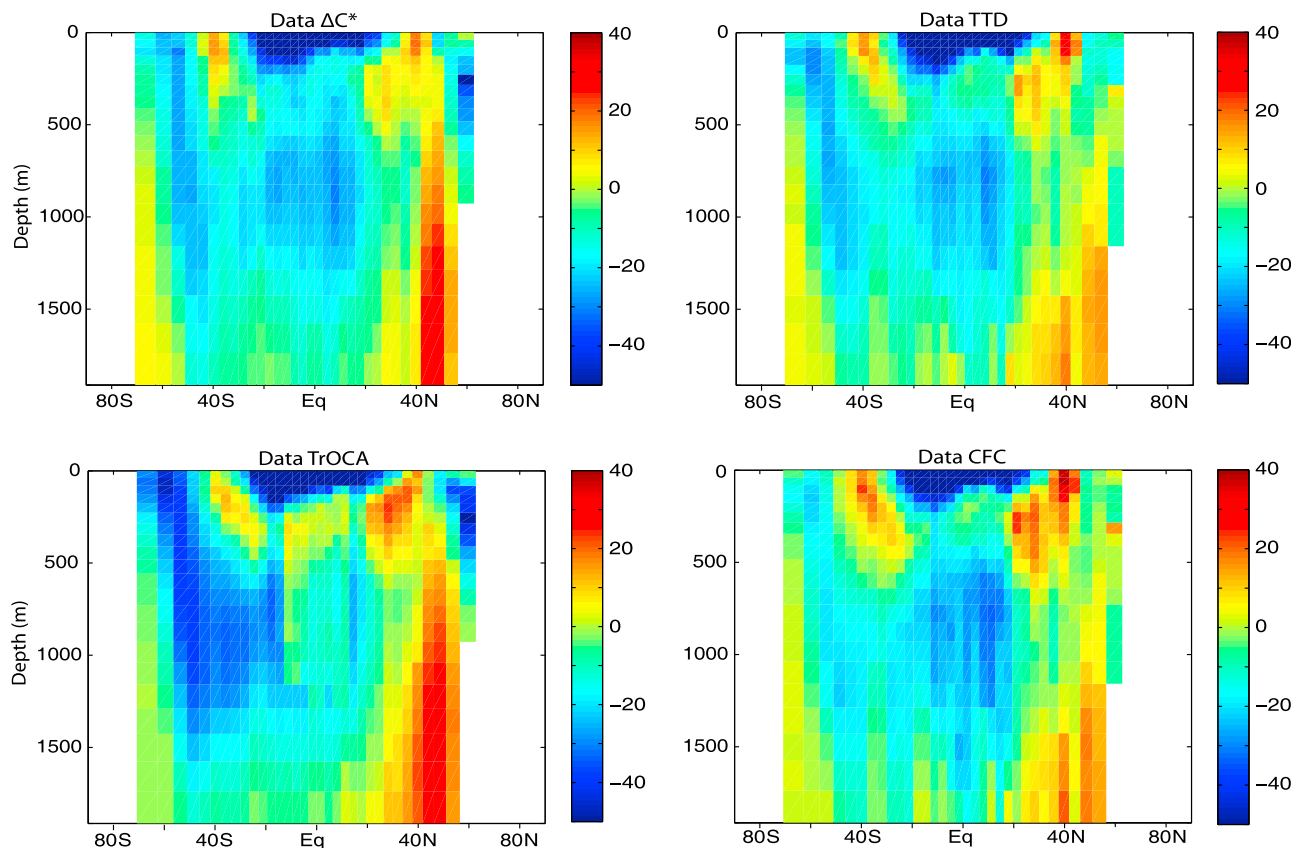
[43] Next, we investigate the sensitivity of the preindustrial air-sea fluxes to the four different ΔC_{gasex} fields. At this stage, we only use the Standard circulation setup of the Bern3D model.

[44] The four ΔC_{gasex} reconstructions differ remarkably. The root-mean-square error (RMSE) between the different ΔC_{gasex} fields ranges from $6.91 \mu\text{mol l}^{-1}$ (between TTD and CFC) to $13.17 \mu\text{mol l}^{-1}$ (between TrOCA and CFC). Figure 3 shows the zonally averaged distribution for each of the four reconstructions in the upper Pacific, a region with high deviations among the different reconstruction. Differences are only due to the use of different C_{anth} reconstructions. Large differences in ΔC_{gasex} of order $20 \mu\text{mol l}^{-1}$ are found in various regions. The TrOCA reconstruction yields higher values in the Pacific equatorial thermocline and lower values in the Pacific AAIW than any of the other three reconstructions. In the North Pacific thermocline around 50°N , ΔC_{gasex} concentrations are higher for the ΔC^* and

Table 3. Regional Net Air-to-Sea Fluxes of Preindustrial, Anthropogenic, and Contemporary CO₂ Inferred With Four Different Reconstructions of Anthropogenic Carbon and the ΔC_{gaseq} Tracer^a

Region	River Derived Outgassing	ΔC^*			TTD			TrOCA			CFC		
		C _{anth}	Natural	Total									
Atlantic N.High Lat.	-0.03 ± 0.01	0.12	0.18	0.27	0.09	0.16	0.22	0.17	0.16	0.30	0.16	0.11	0.24
Atlantic N. Midlat.	-0.01 ± 0.01	0.11	0	0.10	0.08	0.03	0.10	0.15	0	0.14	0.07	0.06	0.12
Atlantic N. Low Lat.	-0.04 ± 0.02	0.04	0.15	0.15	0.06	0.16	0.18	0.01	0.17	0.14	0.06	0.15	0.17
Atlantic N. Tropics	-0.09 ± 0.05	0.03	-0.09	-0.15	0.04	-0.13	-0.18	0.02	-0.10	-0.17	0.03	-0.13	-0.19
Atlantic S. Tropics	-0.02 ± 0.01	0.09	-0.09	-0.02	0.10	-0.09	-0.01	0.15	-0.08	0.05	0.12	-0.10	0
Atlantic S. Low Lat.	0 ± 0	0	0	0	0	0.01	0.01	0.01	-0.01	0	0	0.01	0.01
Atlantic S. Midlat.	-0.01 ± 0	0.08	0.21	0.28	0.07	0.09	0.15	-0.01	0.22	0.20	0.08	0.08	0.15
Pacific N. High Lat.	-0.03 ± 0.01	0.05	-0.01	0.01	0.03	0	0	0.10	0	0.07	0.03	0.02	0.02
Pacific N. Midlat.	-0.05 ± 0.02	0.14	0.25	0.34	0.17	0.23	0.35	0.08	0.29	0.32	0.21	0.23	0.41
Pacific N. Tropics	-0.03 ± 0.01	0.15	-0.29	-0.17	0.21	-0.29	-0.11	0.15	-0.33	-0.21	0.20	-0.30	-0.13
Pacific S. Tropics	-0.01 ± 0.01	0.07	-0.24	-0.18	0.16	-0.25	-0.10	0.09	-0.24	-0.16	0.16	-0.27	-0.12
Pacific S. Midlat.	0 ± 0	0.14	0.48	0.62	0.05	0.50	0.55	0.12	0.58	0.70	0.06	0.54	0.60
Indian Tropics	-0.09 ± 0.04	0.05	-0.11	-0.15	0.06	-0.11	-0.14	0.10	-0.16	-0.15	0.07	-0.11	-0.13
Indian S. Midlat.	-0.01 ± 0.00	0.16	0.26	0.41	0.16	0.23	0.38	-0.03	0.46	0.42	0.17	0.24	0.40
Southern Ocean	-0.01 ± 0.00	0.72	-0.72	-0.01	0.75	-0.54	0.20	1.09	-0.98	0.10	0.88	-0.54	0.33
Global	-0.41 ± 0.21	1.95	-0.01	1.53	2.04	0	1.62	2.20	-0.02	1.77	2.30	-0.01	1.88
Skill score		0.839			0.870			0.760			0.686		
RMSE C _{anth} (μmol Γ ⁻¹)		7.20			6.76			9.85			13.37		
RMSE ΔC _{gaseq} (μmol Γ ⁻¹)		16.86			16.39			19.44			17.21		
Correlation		0.7			0.71			0.67			0.66		

^aUnits are in GtC yr⁻¹. The contemporary air-sea flux is calculated by adding the river-derived outgassing [Jacobson *et al.*, 2007] to the natural and anthropogenic flux. The skill scores and the RMSE for C_{anth} are taken from Gerber *et al.* [2009].

**Figure 3.** Zonal average of data-based ΔC_{gaseq} in $\mu\text{mol } \Gamma^{-1}$ in the upper Pacific for four reconstruction methods.

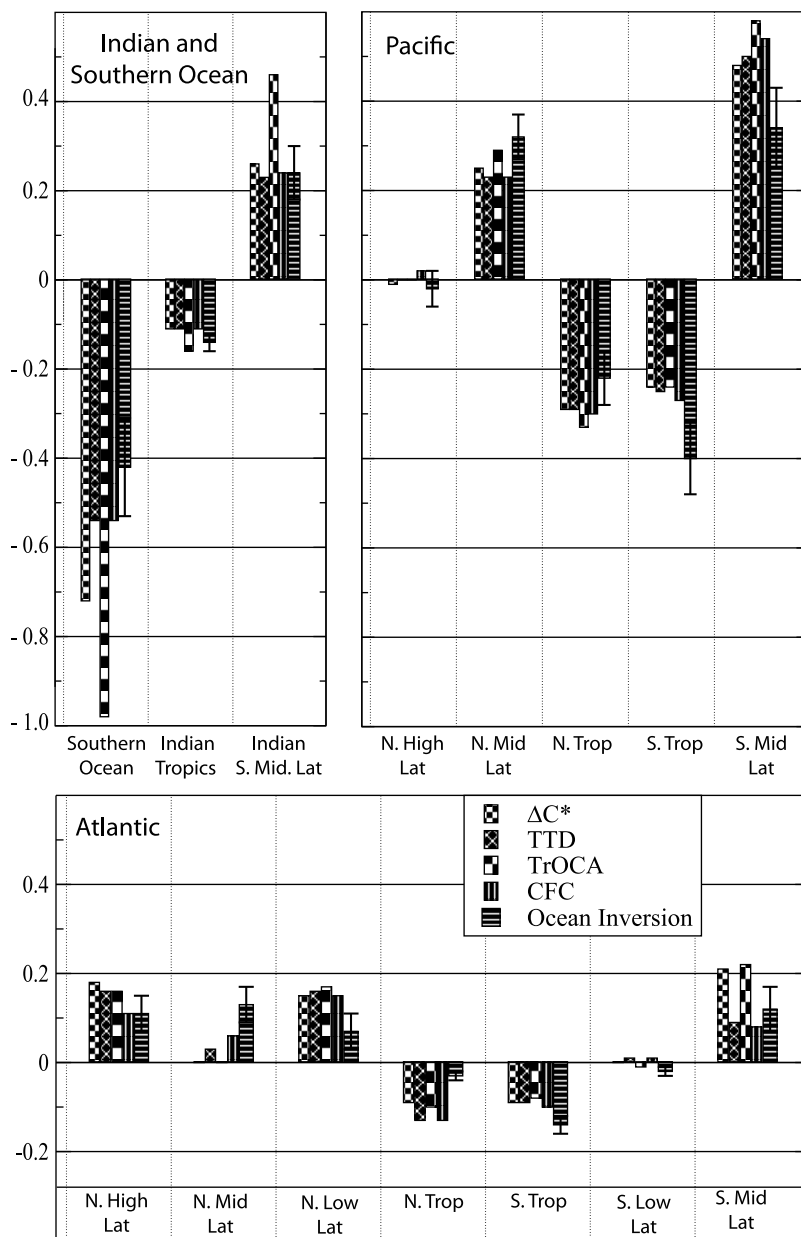


Figure 4. Regional net air-to-sea fluxes in GtC yr^{-1} for four different reconstruction methods compared to the estimates of Mikaloff Fletcher et al. [2007]. The error bar shows the weighted standard deviation of the models participating in the work of Mikaloff Fletcher et al. [2007].

the TrOCA reconstructions than for the TTD and CFC reconstructions; the latter two methods suggest the presence of a substantial amount of anthropogenic carbon in this region. Subtracting this anthropogenic signal from the observed C_T (equation (1)) leads to a lower ΔC_{gasex} concentration than, e.g., derived from the ΔC^* method. Similar differences as in the upper Pacific are also found in the Atlantic.

[45] As with the different circulations, the magnitude of flux in the Southern Ocean, the southern midlatitudes, and in the high-latitude Atlantic are particularly sensitive to the choice of the ΔC_{gasex} fields (Figure S3 and Tables 2 and S2).

For all other regions, deviations are less than 0.06 GtC yr^{-1} . Inferred outgassing in the Southern Ocean varies almost by a factor of 2 for the different reconstructions and ranges from 0.53 (TTD, CFC) to 0.98 GtC yr^{-1} (TrOCA). The TrOCA-based and ΔC^* -based reconstructions yield a higher concentration of C_{anth} and thus a lower ΔC_{gasex} in the AAIW compared to the CFC and TTD reconstructions. This implies a stronger preindustrial Southern Ocean outgassing for the TrOCA and the ΔC^* reconstructions. The TrOCA reconstruction yields also a very high preindustrial uptake flux in the southern midlatitude Indian ocean (Figure 4). The a posteriori flux correlation between the

midlatitude Indian and the Southern Ocean (Figure S4) is quite high, and flux magnitudes for individual regions have to be interpreted carefully. However, the aggregated flux for these two region is still more than 0.2 GtC yr^{-1} higher for the ΔC^* and TrOCA than for the TTD reconstruction.

[46] In conclusion, the explicit consideration of the sensitivity to ΔC_{gasex} input data explains the larger error bars given in this study compared to those estimated by *Gruber et al.* [2009] and *Mikaloff Fletcher et al.* [2007]. Our uncertainties are substantially higher in the Southern Ocean and in southern midlatitudes where uncertainties from the ΔC_{gasex} input data are larger than those from ocean transport. (Table S2).

3.2.3. Sensitivity of Preindustrial Air-Sea Fluxes to the Inversion Method

[47] The Green's function of the Bern3D model have also been used in the inversion of *Mikaloff Fletcher et al.* [2007] allowing us to compare the sensitivity of the flux to the choice of inversion method and experimental details. We use the published data and aggregate the uncertainties using Gaussian error propagation. The regional fluxes are not interpolated to our region map, as the different regions only slightly differ in terms of area.

[48] Surprisingly large differences are found given that the same ΔC_{gasex} data calculation and the same ocean model are applied in both inversions (Table 2). Southern Ocean outgassing is 0.4 GtC yr^{-1} larger in the EnKF inversion than in the GFOI. This increased outgassing might partly be compensated by the increased uptake rates of the EnKF in the southern midlatitudes (0.15 GtC yr^{-1} higher than in GFOI). Large differences between the two approaches are found in the southern tropical Pacific, where the GFOI shows much higher outgassing rates than the EnKF approach (Table 2). We note that the correlation between the air-sea fluxes in the southern midlatitudes and Southern Ocean are quite high, especially the one between the Indian section and the Southern Ocean (Figure S4). This points toward uncertainties in the partitioning of the air-sea fluxes between those regions, however the aggregated fluxes for the southern midlatitudes and high latitudes or for the tropical Pacific differ remarkably between the two approaches. We are not in a position to single out the factors that contribute to these differences in the air-sea fluxes between the two approaches; these are likely linked to differences in setups (resolution of the input data grid, mapping of the regions). However, residuals between assimilated and modeled data may provide an indication [*Mikaloff Fletcher et al.*, 2007, Figures 2 and 7]. Both inversions yield substantial root mean square deviations between assimilated and optimized ΔC_{gasex} for all ocean models and for all experimental setups. The inversions yield a smoother distribution in ΔC_{gasex} with weaker gradients than reconstructed. We have implemented the fluxes from the GFOI in a forward simulation with the Bern3D model and found a root mean square deviation between reconstructed and simulated ΔC_{gasex} field of $18.7 \mu\text{mol l}^{-1}$ compared to the $16.86 \mu\text{mol l}^{-1}$ for EnKF inversion. The difference is likely explained by different weighting of the assimilated data in the GFOI and the EnKF and should not be interpreted as an indication for the quality of the two inversions. Both inversions have difficulties to

represent the reconstructed ΔC_{gasex} and the qualitatively similar flux patterns of the EnKF and of the GFOI yield similar root mean square deviations.

3.2.4. Deviations Between Assimilated and Modeled ΔC_{gasex} Concentrations

[49] The deviation between the reconstructed and modeled ΔC_{gasex} fields are large for all setups (Tables 2 and 3). The RMSE are between 18 (standard) and $14 \mu\text{mol l}^{-1}$ ("PSI $\times 3$ ") for different circulations and between 16 (standard) and $20 \mu\text{mol l}^{-1}$ for the different ΔC_{gasex} reconstruction and standard circulation. The correlation between reconstructed and modeled ΔC_{gasex} fields are between 0.7 (standard) and 0.78 ("PSI $\times 3$ ") and between 0.66 to 0.71 for the different ΔC_{gasex} reconstruction and standard circulation. The TTD reconstruction with the PSI $\times 3$ circulation shows the best agreement in terms of correlation and relative standard deviation [*Taylor, 2001*] between optimized and reconstructed ΔC_{gasex} field. The choice of the circulation setups has a stronger impact on the residuals between modeled and observed distribution than the choice of the reconstruction method. None of the model setups is able to reproduce the observed variance of the ΔC_{gasex} distribution (Figure S5). Correlation coefficients are rather low, the highest achieved correlation is 0.78 (Table 2). The zonally averaged residuals in the Atlantic, Pacific and Indian range between -40 and $+40 \mu\text{mol l}^{-1}$, comparable to reconstructed ΔC_{gasex} range of -60 to $+60 \mu\text{mol l}^{-1}$ (Figure 2). Part of the data-model mismatch is very likely related to deficiencies in the Bern3D transport. Most notable is a too weak formation and northward penetration of AAIW and a too shallow penetration of NADW in the standard setup. However, large residuals and RMSE are not unique to the Bern3D-EnKF assimilation, but have also been found for each of the ten model or model versions used by *Mikaloff Fletcher et al.* [2007] with a reported RMSE range between 16 and $21 \mu\text{mol kg}^{-1}$. These large residuals may point to some fundamental problems with the ΔC_{gasex} tracer.

[50] ΔC_{gasex} is advected and mixed from the surface and has no sources and sinks in the interior ocean implying that concentrations in the interior should be within the concentration range of the source regions. However, interior concentrations often appear to be outside the concentration range of potential source regions. For the ΔC^* reconstruction, concentrations are below $40 \mu\text{mol l}^{-1}$ between 500 and 1000 m, whereas higher concentrations (up to $68 \mu\text{mol l}^{-1}$) are again found at greater depths in the North Atlantic. The relatively high concentrations in the thermocline and the deep northern Pacific in the ΔC^* reconstruction appear also not to be reflected in any of the potential source waters. Concentrations in the deep (>2000 m) Pacific are up to $35 \mu\text{mol l}^{-1}$, whereas concentrations in the Southern Ocean surface and in the deep Indian and in the Atlantic sector of the Southern Ocean are clearly lower. Similarly, the relatively high values of $5 \mu\text{mol l}^{-1}$ in the upper thermocline around 35°S in the Indian and Atlantic appear to have no correspondence in adjacent source regions. As a consequence, the assimilation is not able to match the ΔC_{gasex} concentrations simultaneously. Data-model misfits are also found in the GFOI of *Mikaloff Fletcher et al.* [2007].

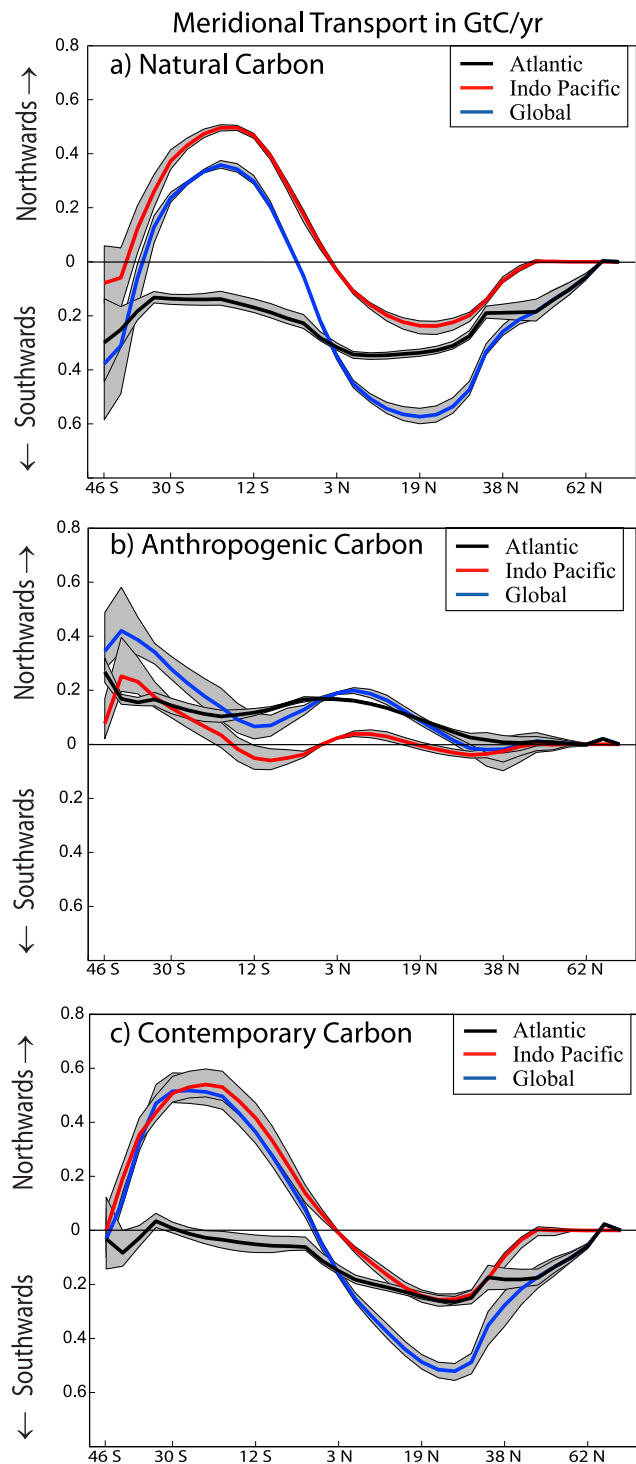


Figure 5. Meridional ocean carbon transport for the (a) preindustrial, (b) anthropogenic perturbation, and (c) present for the global ocean (blue), Atlantic (black), and Indo-Pacific (red). Rates are inferred by assimilating four different reconstructions of C_{anth} and ΔC_{gase} into the standard version of the Bern3D model. Solid lines show best estimates and the shading the spread from the different input data.

[51] How can these apparent inconsistencies in ΔC_{gase} be explained? Nonrepresentative sampling may add uncertainties, but we rely on around 47'000 samples to yield 15897 data points on the Bern3D model grid. Analytical uncertainties in the measurements of C_T , Alk , and PO_4^{3-} are too small and uncertainties in the reconstructed C_{anth} fields can also not explain the data-model mismatch. Potentially important are uncertainties in the Redfield factors used in equation (1). For example, typical concentrations of PO_4^{3-} in the North Pacific are around $3 \mu\text{mol l}^{-1}$. A decrease in $(R_{C:P} + 0.5 \times R_{N:P})$, used in equation (1), by 10% yields an increase in ΔC_{gase} of $37 \mu\text{mol l}^{-1}$. For further discussion we refer to *Matsumoto and Gruber* [2005] and *Mikaloff Fletcher et al.* [2007].

[52] Alternatively, interior concentrations outside the source region may be a consequence of past variability in air-sea CO_2 fluxes or ocean transport, e.g., in response to volcanic eruptions or as part of the internal climate variability [*Frölicher et al.*, 2009].

[53] In summary, large residuals are found for all individual setups. This may point to fundamental problems with the ΔC_{gase} tracer, possibly related to spatial variations in the Redfield ratio between PO_4^{3-} and C_T of order 5 to 10 percent or related to ocean variability.

3.2.5. Meridional Ocean Carbon Transport

[54] Meridional ocean transport rates are linked to the pattern of air-sea gas exchange of CO_2 . Here, we neglect any possible contribution of riverine carbon. Using this assumption, the preindustrial steady state net air-sea flux corresponds to the divergence in transport. The southward transport increases steadily from the northern high latitudes to reach 0.6 GtC yr^{-1} at 19°N . In other words, the temperate and high-latitude Northern Hemisphere ocean absorbs on average 0.6 GtC yr^{-1} at preindustrial times. Maxima in equatorward directed ocean transport are 0.6 GtC yr^{-1} and 0.3 GtC yr^{-1} in the Northern and Southern Hemisphere, supporting a tropical outgassing of 0.9 GtC yr^{-1} . Transport across the equator is small (0.24 GtC yr^{-1}). The carbon uptake in the southern midlatitudes is reflected in the decrease in northward transport by 0.84 GtC yr^{-1} from 19°S to 44°N . The outgassing of the Southern Ocean is supported by a corresponding preindustrial southward transport.

[55] For the individual basins, we infer an extensive preindustrial southward transport of CO_2 throughout the Atlantic (Table S1 and Figure 5), whereas transport rates are equatorward in the Indo-Pacific (north of 40°S). The southward transport in the Atlantic is mainly driven by the formation and export of NADW. In the upper Atlantic (>1000 meter) carbon transport is directed poleward in the northern high latitudes and midlatitudes.

[56] The transport of anthropogenic carbon is primarily northward [see *Gerber et al.*, 2009, Table 4]. The most important transport pathway is from the Southern Ocean to the midlatitudes and subtropics in connection with the northward spreading of AAIW and Subantarctic Mode Water, while transport rates are somewhat smaller in the Northern Hemisphere. A substantial fraction of the anthropogenic carbon taken up in the Southern Ocean is exported to the midlatitudes.

[57] Contemporary meridional ocean carbon transport is directed southward in the Northern Hemisphere and south of 42°S, and northward in the temperate and tropical Southern Hemisphere (Figure 5). The large transport of carbon into the Southern Ocean inferred for the preindustrial state is largely offset by the northward transport of anthropogenic carbon and reduced by about a factor of 3. Here, we neglect any possible contribution from river-derived carbon.

[58] The spread in transport among the different reconstruction methods is small in the tropical regions (0.05 GtC yr⁻¹), but large for the transport from the southern midlatitudes to the Southern Ocean. The range in the contemporary flux into the Southern Ocean region is from zero flux to 0.33 GtC yr⁻¹ across the four different input data sets. The range (0.54 to 0.98 GtC yr⁻¹) is even larger for the preindustrial flux.

[59] In summary, we infer relatively modest meridional transport rates for both the preindustrial and the contemporary ocean and a small carbon transport across the equator. The preindustrial carbon transport into the Southern Ocean is partly offset by the export of anthropogenic carbon out of the Southern Ocean.

4. Discussion and Conclusion

[60] An Ensemble Kalman Filter is combined with the Bern3D ocean model and tracer data to quantify preindustrial, anthropogenic, and contemporary air-sea fluxes of CO₂ and meridional carbon transport within the ocean. The EnKF provides an alternative to other inverse methods such as the Green's function approach or the adjoint methods [Schlitzer, 2002, 2007].

[61] We find a substantial preindustrial outgassing in the tropical and in the Southern Ocean, and carbon uptake in the midlatitudes and northern high latitudes as well as a small interhemispheric carbon transport. The anthropogenic carbon uptake offsets the preindustrial net sea-to-air CO₂ flux in the Southern Ocean, implying that the Southern Ocean is currently on average a weak carbon sink for the atmosphere. The reconstructed contemporary fluxes for broad latitudinal bands are largely consistent with results from Green's function ocean inversions [Gloor *et al.*, 2003; Jacobson *et al.*, 2007; Gruber *et al.*, 2009], the fluxes computed from the surface ocean pCO₂ climatology [Takahashi *et al.*, 2009], and atmospheric inversions [Baker *et al.*, 2006]. However, sensitivity simulations and the analysis of deviations between assimilated and optimized tracer fields reveal large uncertainties in regional air-sea flux, in particular for the Southern Ocean. Improvements in quantification and understanding of Southern Ocean processes is high on the research agenda as this region plays a critical role for the fate of anthropogenic carbon and for the glacial-interglacial CO₂ variations.

[62] The reconstruction of anthropogenic carbon is a potential source of biases in the estimates of ΔC_{gasex} . Another bias may be imposed by the normalization of the ΔC_{gasex} field. Regional air-sea fluxes from the EnKF assimilations are compared to those inferred from observations of the air-sea CO₂ partial pressure differences [Takahashi *et al.*, 2009]. Overall, best agreement is found when relying on the TTD reconstruction [Waugh *et al.*,

2006] in the EnKF assimilation. The explicit consideration of uncertainties in the reconstructions of C_{anth} and ΔC_{gasex} explains the larger error bars given in this study compared to those estimated by Gruber *et al.* [2009] and Mikaloff Fletcher *et al.* [2007].

[63] Optimized air-sea fluxes are also sensitive to the choice of the inversion method. For example, preindustrial outgassing in the Southern Ocean is with 0.7 GtC yr⁻¹ more than twice as large in the EnKF inversion than in the corresponding Green's function inversion when applying the same ocean model and ΔC_{gasex} data calculation. This suggests that the air-sea fluxes are not tightly constrained by the assimilated data and details of the inversion methods matter.

[64] Large root mean square deviations between the assimilated and the optimized ΔC_{gasex} fields of 15 to 20 $\mu\text{mol l}^{-1}$ are found for all individual setups of this study or by Mikaloff Fletcher *et al.* [2007] who applied ten different models and model versions in their Green's function inversion. The range of zonal mean residuals in ΔC_{gasex} is comparable to the reconstructed range in ΔC_{gasex} . The inversions yield a much smoother distribution in ΔC_{gasex} and gradients are much weaker than reconstructed. This may point to fundamental problems with the ΔC_{gasex} tracer, possibly related to spatial variations in the stoichiometric ratios between phosphate and carbon of order 5 to 10 percent or related to ocean variability. These two factors should be more explicitly addressed in future work.

[65] Another source of uncertainties is related to the representation of ocean transport processes. Small-scale features such as eddies and convection or the formation of Antarctic Bottom Water (AABW) on the shelves around Antarctica are not explicitly represented in the Bern3D model nor in the current crop of global ocean models. An inadequate representation of transport processes in the model may lead to a mismatch between modeled transport and the prescribed observation-based gas exchange pattern. This may affect the inverse estimates. However, air-sea fluxes of C_{anth} are only slightly sensitive to the choice of the underlying air-sea flux pattern as an experiment with spatial and temporal constant air-sea flux pattern has revealed. Results of forward simulations with eddy resolving model for transient tracers have recently become available [Lachkar *et al.*, 2007; Ito *et al.*, 2010]. The results of these studies do not point to fundamentally different large-scale transport pathways compared to coarse resolution models, though Southern Ocean stratification is much better represented and excessive mixing suppressed in the high-resolution models. Comparing a transient tracer forward simulation with an eddy-permitting and a coarse resolution model version, Lachkar *et al.* [2007] found a decrease in air-sea flux and inventory of C_{anth} in the Southern Ocean of 23% and 35%, respectively. It remains the task for the future to apply high-resolution transport models for the assimilation of biogeochemical data.

[66] In conclusion, oceanic tracer data have been successfully assimilated with an Ensemble Kalman Filter to quantify regional air-sea fluxes and meridional ocean transport of carbon. Results for the Southern Ocean, southern midlatitudes and the northern North Atlantic regions

are particularly sensitive to uncertainties in input data, to uncertainties in ocean transport, and to the choice of inverse method and experimental details. Estimated uncertainties in input data are larger than uncertainties in ocean transport in the high-latitude and midlatitude Southern Hemisphere. Systematic differences in assimilated and optimized ΔC_{gasex} fields remain uncomfortably large, suggesting that the error estimates given in this study represent lower bounds. The contemporary, anthropogenic, and preindustrial air-sea CO_2 flux in the Southern Ocean remain uncertain.

[67] **Acknowledgments.** We acknowledge Andy Jacobson, Sara Mikaloff Fletcher, Neil Edwards, and Niki Gruber for fruitful comments and discussions regarding this work. This study was financially supported by the European Union through the Integrated Project CarboOcean (511106-2), the Swiss National Science Foundation, and the Swiss Staatssekretariat für Bildung und Forschung (C07.0068; COST Action 735).

References

- Álvarez, M., et al. (2009), Estimating the storage of anthropogenic carbon in the subtropical Indian ocean: A comparison of five different approaches, *Biogeosci. Disc.*, 6(1), 729–796.
- Anderson, L. A., and J. L. Sarmiento (1994), Redfield ratios of remineralization determined by nutrient data analysis, *Global Biogeochem. Cycles*, 8(1), 65–80.
- Baker, D. F., et al. (2006), Transcom 3 inversion intercomparison: Impact of transport model errors on the interannual variability of regional CO_2 fluxes 1988–2003, *Global Biogeochem. Cycles*, 20, GB1002, doi:10.1029/2004GB002439.
- Bakker, D., J. Etcheto, J. Boutin, and L. Merlivat (2001), Variability of surface water fCO_2 during seasonal upwelling in the equatorial Atlantic Ocean as observed by a drifting buoy, *J. Geophys. Res.*, 106(C5), 9241–9253.
- Chen, C. T. A., and F. J. Millero (1979), Gradual increase of oceanic CO_2 , *Nature*, 277, 205–206.
- Denman, K. L., et al. (2007), Couplings between changes in the climate system and biogeochemistry, in *Climate Change 2007: The Physical Science Basis. Working Group I Contribution to the Fourth Assessment Report of the Intergovernmental Panel on Climate Change*, edited by S. Solomon et al., pp. 499–588, Cambridge Univ. Press, Cambridge, U. K.
- Edwards, N. R., and R. Marsh (2005), Uncertainties due to transport-parameter sensitivity in an efficient 3-D ocean-climate model, *Clim. Dyn.*, 24(4), 415–433, doi:10.1007/s00382-004-0508-8.
- Enting, I. G., and J. V. Mansbridge (1989), Seasonal sources and sinks of atmospheric CO_2 : Direct inversion of filtered data, *Tellus, Ser. B*, 41(2), 11–126.
- Evensen, G. (2003), The Ensemble Kalman Filter: Theoretical formulation and practical implementation, *Ocean Dyn.*, 53, 343–367.
- Evensen, G. (2004), Sampling strategies and square root analysis schemes for the EnKF, *Ocean Dyn.*, 54, 539–560.
- Frölicher, T. L., F. Joos, G.-K. Plattner, M. Steinacher, and S. C. Doney (2009), Natural variability and anthropogenic trends in oceanic oxygen in a coupled carbon cycle-climate model ensemble, *Global Biogeochem. Cycles*, 23, GB1003, doi:10.1029/2008GB003316.
- Gerber, M., F. Joos, M. Vázquez Rodríguez, F. Touratier, and C. Goyet (2009), Regional air-sea fluxes of anthropogenic carbon inferred with an Ensemble Kalman Filter, *Global Biogeochem. Cycles*, 23, GB1013, doi:10.1029/2008GB003247.
- Gloor, M., N. Gruber, J. L. Sarmiento, C. L. Sabine, R. A. Feely, and C. Rödenbeck (2003), A first estimate of present and preindustrial air-sea CO_2 flux patterns based on ocean interior carbon measurements and models, *Geophys. Res. Lett.*, 30(1), 1010, doi:10.1029/2002GL015594.
- Gruber, N., and J. L. Sarmiento (2002), Biogeochemical/physical interactions in elemental cycles, in *The Sea: Biological-Physical Interactions in the Oceans*, vol. 12, edited by A. R. Robinson, J. J. McCarthy, and B. J. Rothschild, pp. 337–399, John Wiley.
- Gruber, N., J. Sarmiento, and T. F. Stocker (1996), An improved method for detecting anthropogenic CO_2 in the oceans, *Global Biogeochem. Cycles*, 10(4), 809–837.
- Gruber, N., et al. (2009), Oceanic sources, sinks, and transport of atmospheric CO_2 , *Global Biogeochem. Cycles*, 23, GB1005, doi:10.1029/2008GB003349.
- Heimann, M., and E. Maier-Reimer (1996), On the relations between the oceanic uptake of CO_2 and its carbon isotopes, *Global Biogeochem. Cycles*, 10(1), 89–110.
- Ito, T., M. Woloszyn, and M. Mazloff (2010), Anthropogenic carbon dioxide transport in the Southern Ocean driven by Ekman flow, *Nature*, 463, 80–83, doi:10.1038/nature08687.
- Jacobson, A. R., S. E. Mikaloff Fletcher, N. Gruber, J. L. Sarmiento, and M. Gloor (2007), A joint atmosphere-ocean inversion for surface fluxes of carbon dioxide: 1. methods and global-scale fluxes, *Global Biogeochem. Cycles*, 21, GB1019, doi:10.1029/2005GB002556.
- Joos, F., and R. Spahni (2008), Rates of change in natural and anthropogenic radiative forcing over the past 20,000 years, *Proc. Natl. Acad. Sci. U. S. A.*, 105(5), 1425–1430.
- Kaminski, T., M. Heimann, P. Peylin, P. Bousquet, and P. Ciais (2001), Inverse modeling of atmospheric carbon dioxide fluxes, *Science*, 294(5541), 259, doi:10.1126/science.294.5541.259a.
- Key, R. M., A. Kozyr, C. L. Sabine, K. Lee, R. Wanninkhof, J. L. Bullister, R. A. Feely, F. J. Millero, C. Mordy, and T.-H. Peng (2004), A global ocean carbon climatology: Results from Global Data Analysis Project (GLODAP), *Global Biogeochem. Cycles*, 18, GB4031, doi:10.1029/2004GB002247.
- Lachkar, Z., J. C. Orr, J.-C. Dutay, and P. Delecluse (2007), Effects of mesoscale eddies on global ocean distributions of CFC-11, CO_2 , and $\Delta^{14}\text{C}$, *Ocean Sci.*, 3(4), 461–482.
- Lüthi, D., et al. (2008), High-resolution carbon dioxide concentration record 650,000–800,000 years before present, *Nature*, 453, 379–382, doi:10.1038/nature06949.
- Maier-Reimer, E. (1993), Geochemical cycles in an ocean general circulation model. Preindustrial tracer distributions, *Global Biogeochem. Cycles*, 7(3), 645–677.
- Matear, R. J., C. S. Wong, and L. Xie (2003), Can CFCs be used to determine anthropogenic CO_2 ?, *Global Biogeochem. Cycles*, 17(1), 1013, doi:10.1029/2001GB001415.
- Matsumoto, K., and N. Gruber (2005), How accurate is the estimation of anthropogenic carbon in the ocean? An evaluation of the ΔC^* method, *Global Biogeochem. Cycles*, 19, GB3014, doi:10.1029/2004GB002397.
- Mikaloff Fletcher, S. E., et al. (2006), Inverse estimates of anthropogenic CO_2 uptake, transport, and storage by the ocean, *Global Biogeochem. Cycles*, 20, GB2002, doi:10.1029/2005GB002530.
- Mikaloff Fletcher, S. E., et al. (2007), Inverse estimate of the oceanic sources and sinks of natural CO_2 and the implied oceanic carbon transport, *Global Biogeochem. Cycles*, 21, GB1010, doi:10.1029/2006GB002751.
- Müller, S. A., F. Joos, N. R. Edwards, and T. F. Stocker (2006), Water mass distribution and ventilation time scales in a cost-efficient, three-dimensional ocean model, *J. Clim.*, 19(21), 5479–5499.
- Müller, S. A., F. Joos, G.-K. Plattner, N. R. Edwards, and T. F. Stocker (2008), Modeled natural and excess radiocarbon: Sensitivities to the gas exchange formulation and ocean transport strength, *Global Biogeochem. Cycles*, 22, GB3011, doi:10.1029/2007GB003065.
- Murnane, R., J. Sarmiento, and C. LeQuéré (1999), Spatial distribution of air-sea CO_2 fluxes and the interhemispheric transport of carbon by the oceans, *Global Biogeochem. Cycles*, 13(2), 287–305.
- Parekh, P., F. Joos, and S. A. Müller (2008), A modeling assessment of the interplay between aeolian iron fluxes and iron-binding ligands in controlling carbon dioxide fluctuations during Antarctic warm events, *Paleoceanography*, 23, PA4202, doi:10.1029/2007PA001531.
- Rödenbeck, C., C. Le Quéré, M. M. Heimann, and R. F. Keeling (2008), Interannual variability in oceanic biogeochemical processes inferred by inversion of atmospheric O_2/N_2 and CO_2 data, *Tellus, Ser. B*, 60(5), 685–705.
- Sabine, C. L., et al. (2004), The oceanic sink for anthropogenic CO_2 , *Science*, 305(5682), 367–371, doi:10.1126/science.1097403.
- Sarmiento, J. L., and E. T. Sundquist (1992), Revised budget for the oceanic uptake of anthropogenic carbon dioxide, *Nature*, 356, 589–593, doi:10.1038/356589a0.
- Sarmiento, J., P. Monfray, E. Maier-Reimer, O. Aumont, R. Murnane, and J. Orr (2000), Sea-air CO_2 fluxes and carbon transport: A comparison of three ocean general circulation models, *Global Biogeochem. Cycles*, 14(4), 1267–1281.
- Schlitzer, R. (2002), Carbon export fluxes in the Southern Ocean: Results from inverse modeling and comparison with satellite-based estimates, *Deep Sea Res., Part II*, 49, 1623–1644.

- Schlitzer, R. (2007), Assimilation of radiocarbon and chlorofluorocarbon data to constrain deep and bottom water transports in the world ocean, *J. Phys. Oceanogr.*, 37(2), 259–276.
- Takahashi, T., et al. (2002), Global sea-air CO₂ flux based on climatological surface ocean pCO₂, and seasonal biological and temperature effects, *Deep Sea Res., Part II*, 49, 1601–1622.
- Takahashi, T., et al. (2009), Climatological mean and decadal changes in surface ocean pCO₂, and net sea-air CO₂ flux over the global oceans, *Deep Sea Res., Part II*, 10(8–10), 554–577, doi:10.1016/j.dsr2.2008.12.009.
- Tans, P. P., I. Y. Fung, and T. Takahashi (1990), Observational constraints on the global atmospheric CO₂ budget, *Science*, 247, 1431–1439, doi:10.1126/science.247.4949.1431.
- Taylor, K. E. (2001), Summarizing multiple aspects of model performance in a single diagram, *J. Geophys. Res.*, 106(D7), 7183–7192.
- Thomas, H., and V. Ittekkot (2001), Determination of anthropogenic CO₂ in the North Atlantic Ocean using water mass ages and CO₂ equilibrium chemistry, *J. Mar. Syst.*, 27(12), 325–336, doi:10.1016/S0924-7963(00)00077-4.
- Touratier, F., L. Azouzi, and C. Goyet (2007), CFC-11, 14C and 3H tracers as a means to assess anthropogenic CO₂ concentrations in the ocean, *Tellus, Ser. B*, 59, 318–325, doi:10.1111/j.1600-0889.2006.00247.x.
- Tschumi, T., F. Joos, and P. Parekh (2008), How important are Southern Hemisphere wind changes for low glacial carbon dioxide? A model study, *Paleoceanography*, 23, PA4208, doi:10.1029/2008PA001592.
- Vázquez Rodríguez, M., F. Touratier, C. LoMonaco, D. W. Waugh, X. A. Padin, R. J. Bellerby, C. Goyet, N. Metzel, A. F. Ríos, and F. F. Perez (2009), Anthropogenic carbon distributions in the Atlantic Ocean: Data-based estimates from the Arctic to the Antarctic, *Biogeosciences*, 6, 439–451.
- Volk, T., and M. I. Hoffert (1985), Ocean carbon pumps: Analysis of relative strengths and efficiencies in ocean-driven atmospheric CO₂ changes, in *The Carbon Cycle and Atmospheric CO₂: Natural Variations Archean to Present*, *Geophys. Monogr. Ser.*, vol. 32, edited by E. T. Sundquist and W. S. Broecker, pp. 99–110, AGU, Washington, D. C.
- Wanninkhof, R. (1992), Relationship between wind speed and gas exchange over the ocean, *J. Geophys. Res.*, 97, 7373–7382.
- Waugh, D. W., T. W. N. Haine, and T. M. Hall (2004), Transport times and anthropogenic carbon in the subpolar North Atlantic Ocean, *Deep Sea Res., Part I*, 51(11), 1475–1491, doi:10.1016/j.physletb.2003.10.071.
- Waugh, D. W., T. M. Hall, B. I. McNeil, R. Key, and R. Matear (2006), Anthropogenic CO₂ in the oceans estimated using transit-time distributions, *Tellus, Ser. B*, 58, 376–390, doi:10.1111/j.1600-0889.2006.00222.x.

M. Gerber and F. Joos, Climate and Environmental Physics, Physics Institute, University of Bern, CH-3012 Bern, Switzerland. (mgerber@climate.unibe.ch)